The Journal of Chemical Physics

Self-assembly and entropic effects in pear-shaped colloid systems. I. Shape sensitivity of bilayer phases in colloidal pear-shaped particle systems

Cite as: J. Chem. Phys. **153**, 034903 (2020); https://doi.org/10.1063/5.0007286
Submitted: 11 March 2020 . Accepted: 17 May 2020 . Published Online: 20 July 2020

Philipp W. A. Schönhöfer, Matthieu Marechal, Douglas J. Cleaver, and Gerd E. Schröder-Turk

ARTICLES YOU MAY BE INTERESTED IN

The Journal of Chemical Physics ARTICLE scitation.org/journal/jcp

Self-assembly and entropic effects in pear-shaped colloid systems. I. Shape sensitivity of bilayer phases in colloidal pear-shaped particle systems

Cite as: J. Chem. Phys. **153**, 034903 (2020); doi: 10.1063/5.0007286
Submitted: 11 March 2020 • Accepted: 17 May 2020 •
Published Online: 20 July 2020

Philipp W. A. Schönhöfer,[1,2,a)] **Matthieu Marechal,**[2] **Douglas J. Cleaver,**[3] **and Gerd E. Schröder-Turk**[1,4,b)]

AFFILIATIONS

[1] College of Science, Health, Engineering and Education, Mathematics and Statistics, Murdoch University, 90 South Street, 6150 Murdoch, WA, Australia
[2] Institut für Theoretische Physik I, Friedrich-Alexander-Universität Erlangen-Nürnberg, Staudtstraße 7, 91058 Erlangen, Germany
[3] Materials and Engineering Research Institute, Sheffield Hallam University, Sheffield S1 1WB, United Kingdom
[4] Department of Applied Mathematics, Research School of Physical Sciences and Engineering, The Australian National University, 0200 Canberra, ACT, Australia; Department of Food Science, University of Copenhagen, Rolighedsvej 26, 1958 Frederiksberg C, Denmark; and Physical Chemistry, Center for Chemistry and Chemical Engineering, Lund University, Lund 22100, Sweden

[a)] **Author to whom correspondence should be addressed:** Philipp.Schoenhoefer@fau.de
[b)] G.Schroeder-Turk@murdoch.edu.au

ABSTRACT

The role of particle shape in self-assembly processes is a double-edged sword. On the one hand, particle shape and particle elongation are often considered the most fundamental determinants of soft matter structure formation. On the other hand, structure formation is often highly sensitive to details of shape. Here, we address the question of particle shape sensitivity for the self-assembly of hard pear-shaped particles by studying two models for this system: (a) the pear hard Gaussian overlap (PHGO) and (b) the hard pears of revolution (HPR) model. Hard pear-shaped particles, given by the PHGO model, are known to form a bicontinuous gyroid phase spontaneously. However, this model does not replicate an additive object perfectly and, hence, varies slightly in shape from a "true" pear-shape. Therefore, we investigate in the first part of this series the stability of the gyroid phase in pear-shaped particle systems. We show, based on the HPR phase diagram, that the gyroid phase does not form in pears with such a "true" hard pear-shaped potential. Moreover, we acquire first indications from the HPR and PHGO pair-correlation functions that the formation of the gyroid is probably attributed to the small non-additive properties of the PHGO potential.

I. INTRODUCTION

In colloidal and soft matter science, the influence of particle shape on the geometry of self-assembled meso-structures and, hence, on their physical properties is well documented. To some approximation, colloids behave as hard particles that are subject to thermal Brownian motion. Similar to objects with hard-core potentials, they interact largely by volume exclusion effects, which are defined by their outline, and otherwise feel no energetic repulsion or attraction. The effect of shape is demonstrated, for instance, in dense collections of elongated nano- or microrods, which spontaneously develop a preferential particle direction and, consequently, introduce a distinguished global orientation known as the nematic director.[1,2] Furthermore, it has been reported that the morphology of platonic and other polyhedral colloids can be used as a tool to create complex crystalline arrangements.[3–9] Hence, the manipulation of particle shapes is an auspicious mechanism to design self-assembled materials. However, the relationship between the shape of the constituent particles and the adopted self-assembled structure is not straightforward. While particle shape is beyond doubt an important determinant of structure formation, only a handful of quantifiable shape parameters could be related to long-ranged order directly. In colloidal self-assembly, it is generally accepted that the nematic order only occurs in particles that are sufficiently elongated, indicated by the aspect ratio between the length and width of the particle.[1,6,10–12] Similarly, it has been shown that close-packed structures, like those based on the γ-brass lattice, require particles with a high isoperimetric quotient, which indicates the ratio between the particle's volume and its surface area.[6]

In this article, we focus on a related aspect, namely, shape sensitivity upon self-assembly, which aggravates the prediction of collective behavior in multi-particle systems by just the outline of the single constituents even further. Even if morphological parameters are identified necessary for the formation of certain mesostructures, the stability of these assemblies tends to be sensitive toward small changes in shape. The sensitivity to details of shape is presumably most clearly observed in hard-core systems. These systems are by design reduced to the shape of the inherent particles, which is defined by the hard interaction potentials. Already introducing a small degree of polydispersity into simple systems such as the hard sphere fluid[13] can destabilize the crystalline into an amorphous phase for high densities.[14] Similarly in other hard particle mixtures, where depletion attractions between hard colloidal particles are induced by a solvent of surrounding small depletants, entropic forces are highly affected by the shape of colloids[15–21] (for a more in-depth discussion about depletion, see Paper II[22]). The significant influence of shape also becomes apparent by comparing the phase behavior of hard spherocylinders[1] and hard ellipsoids[2] obtained by simulations. Even though the shapes of the individual particles seem similar, the smectic phase is only assembled by spherocylinders and not by ellipsoids.

These observations are in accordance with other hard particle systems, which have been studied by investigating the intermediate stages of interpolations between two shapes. It has been shown, for example, that in systems of hard cubes, rounded edges have a significant influence on the cubical ordering of the crystalline phase.[4,23–25] In addition to these superballs, various families of truncated polyhedra,[5–9] elongated and twisted triangular prisms,[26] disks with adjustable thickness,[27] and very recently dimpled spheres with various dimple sizes[28] have also been studied. Here, it has been indicated that, in particular, more complex particle arrangements are stable within a narrow window of shapes, which makes them even more prone to small shape changes.

Cubic structures based on triply periodic minimal surfaces are among the most complex representatives of such phases, which have been observed within the field of colloidal self-assembly. For instance, computational simulations of hard pear-shaped particles, reminiscent of tapered ellipsoids, indicate the spontaneous formation of highly symmetric liquid crystal phases, such as the cubic and bicontinuous Ia$\bar{3}$d double gyroid[29,30] or the Pn$\bar{3}$m double diamond phase (upon addition of a hard sphere solvent).[31] Here, the

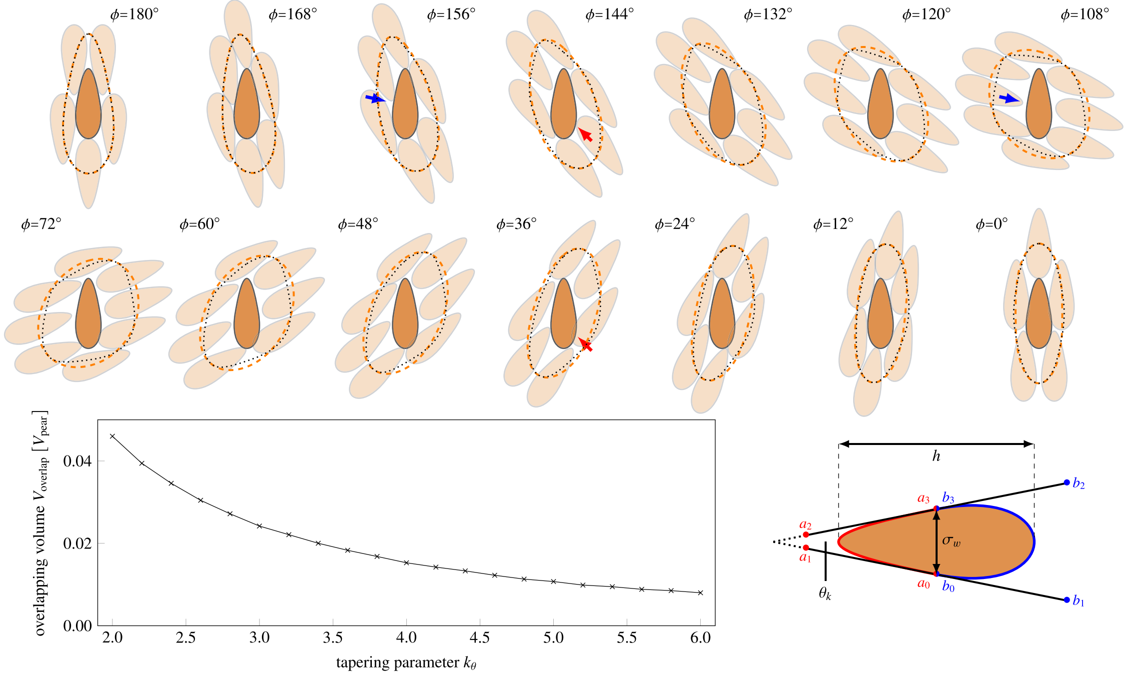

FIG. 1. Top: the contact profiles according to the PHGO model (- -) and the HPR model (....) for identical pear-shaped particles with $k = \frac{h}{\sigma_w} = 3$ and $k_\theta = \left(2\tan\left(\frac{\theta_k}{2}\right)\right)^{-1} = 3$ at different angles between the molecules $\phi = \arccos(\mathbf{u}_i \cdot \mathbf{u}_j)$ in the xz-plane. The surrounding pears are positioned in contact according to the PHGO model. The arrows demonstrate the different contact between blunt (red) and pointy (blue) ends depending on ϕ. Bottom: the maximal overlap volume V_{overlap} between two PHGO particles with different tapering parameters k_θ when in contact. The volume is given in comparison to the volume of the Bézier pear V_{pear}. The marks a_i and b_i are the control points of the Bézier curves, which are used to fit the pear shape.

shape of the used hard-core potential, called the pear hard Gaussian overlap (PHGO) potential, is best illustrated by a pear shape, which is described by two Bézier curves[32] (see Fig. 1 for the outline of a pear-shaped particle). The Bézier curves feature the two main morphological traits of the pear shape: the aspect ratio k between height and width of the colloid and the tapering angle θ_k or the tapering parameter k_θ that encodes the angle between the tangents at the waist of the outline of the pear-shape (see also Fig. 1). However, the effective shape of the PHGO model is just a close approximation and not a perfect fit to the Bézier description. Therefore, the shape represented by the PHGO potential can be interpreted as a slight distortion of the perfect Bézier pear. For a more detailed description of the shape and the PHGO potential, we refer to Refs. 30 and 32.

Up to this point, the influence of the distinctions between the PHGO model and the "true" Bézier pear-shape has not been studied in detail, *a fortiori*, as for the ellipsoidal counterparts [the hard Gaussian overlap (HGO) ellipsoids and the hard ellipsoids of revolution (HER)], small differences between the two models are known.[33] The phase transitions between the isotropic and orientationally ordered liquid crystal phases do not match perfectly for both ellipsoid models as the HGO interaction profile promotes the alignment of particles by a greater margin. Consequently, the phase transition of the HGO ellipsoids occurs for lower densities than for HER ellipsoids. Nevertheless, the distinct transition density does not change the characteristics of the observed phase behavior significantly. Both models exhibit a similar nematic phase in between the isotropic and solid states without the HGO ellipsoids adding more complex phases. Thus, the two types of ellipsoids are qualitatively equivalent, and their small differences in particle-shape are of only marginal consequences. However, the double gyroid phase is a much more complex structure than the "simple" nematic.

It seems plausible that higher complexity leads to an increased response and that, in particular, the self-assembly of configurations such as the double gyroid is more sensitive to the interaction of the particles. Hence, we focus in this paper on the phase behavior of a more accurate, but computationally much more expensive Bézier pear model. In this case, the hard potential is based on triangulated meshes of the pear-surface, which we address as the hard pears of revolution (HPR) model. Here, the contact is determined by testing for the overlap between the triangulated surfaces and, hence, coincides with the Bézier description arbitrarily accurately.

In the following, we first detail the specific shape differences between the two pear-shaped particle models in Sec. II. Afterward, we analyze the effect of these distinctions by calculating the phase diagram of the HPR model numerically and comparing it to the phase behavior of PHGO particles in Sec. III. Here, we show that the gyroid phase, which can be interpreted as a warped bilayer phase, is not universal for tapered pear particles and that the special features of the PHGO contact function promote the formation of otherwise unfavorable bilayer-configurations. Subsequently in Sec. IV, we analyze the local environment of the pear-shaped particles within the different phases. In combination with our results from Paper II, where we observe the depletion behavior between pear-shaped particles within a hard sphere solvent,[22] this study sheds light on the different mesoscopic behavior between the PHGO and HPR model from a microscopic perspective.

II. MICROSCOPIC DIFFERENCES BETWEEN HARD PEARS OF REVOLUTION AND PEAR HARD GAUSSIAN OVERLAP PARTICLES

In Fig. 1, the contact profiles of PHGO and HPR particles with aspect ratio $k = 3$ and tapering parameter $k_\theta = 3$ are compared. The contact profile is determined by the interface of the excluded volume given by the contact function,

$$\sigma(\mathbf{r}_{ij}, \mathbf{u}_i, \mathbf{u}_j) = \begin{cases} 0, & \text{if particles } i \text{ and } j \text{ do not overlap} \\ 1, & \text{if particles } i \text{ and } j \text{ overlap} \end{cases} \tag{1}$$

with the relative distance $\mathbf{r}_{ij}$ between the reference particle i and a secondary particle j and their orientation vectors $\mathbf{u}_i$ and $\mathbf{u}_j$. It becomes apparent that the two models show considerable differences for relative angles $\phi = \arccos(\mathbf{u}_i \cdot \mathbf{u}_j)$ between 50° and 130°. In this regime, the PHGO profile often overestimates the overlap, which leads to gaps between the particles. This, however, is inherited from a similar error between the HGO and HER (hard ellipsoids of revolution) potential of the ellipsoid.[33] For small angles, an additional effect occurs. At around 30°, the PHGO profile also occasionally underestimates the contact distance, in other words, the distance of the closest approach, σ, compared to the Bézier shape such that the colloidal particles overlap with their blunt ends when represented by Bézier pears. The gap size and the overlap volume (see Fig. 1) are higher for more asymmetrical pears such that the PHGO approximation is worse for Bézier-pears with a larger taper.

In the following, we will use the term *self-non-additivity* to describe this combination between over- and underestimation of the contact distance and this special angle dependency of the contact distance. Conventionally, hard-core interactions are labeled additive, if in a mixture the distance of the closest approach σ_{AB} between species A and B can be logically deduced from the contact distance between particles of the same type by the additive constraint: $\sigma_{AB} = 0.5(\sigma_{AA} + \sigma_{BB})$. If this rule does not hold, the mixture is referred to as non-additive.[34–38] This concept is illustrated in Fig. 2(a).

A similar effect, however, also occurs in the mono-disperse PHGO particle system. This becomes apparent by explaining the choice of the prefix "self" in self-non-additivity, which is illustrated by analyzing the contact distance between the blunt ends of the pear-shaped particles in Fig. 1 and explained additionally in Fig. 2(b). For certain relative angles, the blunt ends overlap ($\phi = 36°$), whereas for other angles, their contact coincides with the Bézier description ($\phi = 144°$, indicated by red arrows in Fig. 1). Similar behavior is observed for the contact between the thin ends (gaps at $\phi = 108°$ and no gap at $\phi = 156°$, indicated by blue arrows in Fig. 1). Hence, the PHGO model represents the hard interactions between two Bézier pear-shaped objects depending on their relative angle differently well. Alternatively, differently orientated pears can be interpreted as distinct hard particle species with non-additive interactions as the contact at $\phi = 36°$ cannot be deduced additively form the contact at $\phi = 144°$ [see Fig. 2(b)]. Moreover, the described angular dependency of the contact function implies that a true physical hard shape cannot copy the PHGO model.[39]

Evidently, the self-non-additivity of the PHGO model is a specific form of an orientation- and distance-dependent interaction potential. The interaction remains, for all relative orientations of the

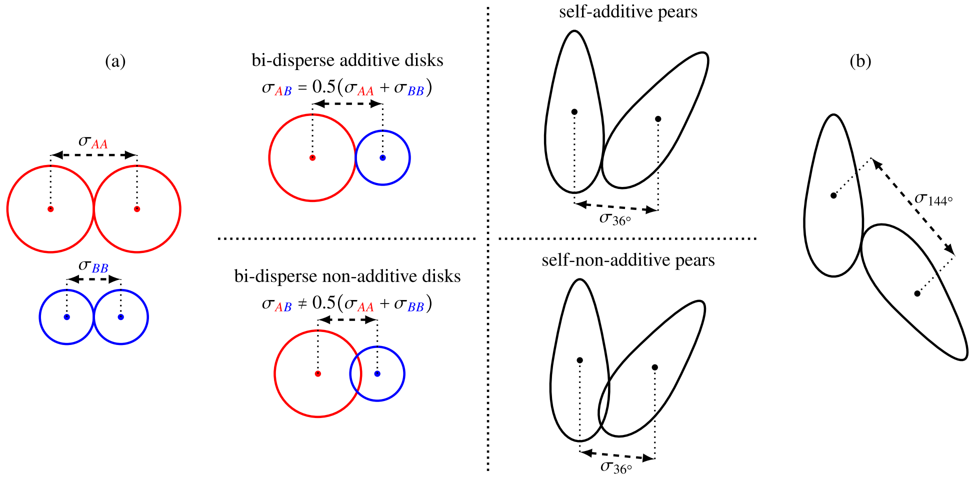

FIG. 2. (a) The concept of an additive and non-additive mixture of disk species *A* and *B*. In the additive mixture, the interspecies contact distance σ_{AB} can be calculated from the contact between disks of the same species σ_{AA} and σ_{BB} by an additive rule. In the non-additive case, this rule does not hold. (b) The concept of self-additive and self-non-additive systems by the example of pear-shaped particles. The contact between different parts of self-additive pears at a certain relative angle (i.e., $\phi = 36°$) and distance can be deduced logically from the contact between the same particles at a different angle (i.e., $\phi = 144°$). In self-non-additive systems, the contact distance between parts of the particles varies and does not follow an overall shape.

particles, a hard-core interaction where the particles experience no interaction until the point of contact.

III. PHASE BEHAVIOR OF HARD PEARS OF REVOLUTION AND PEAR HARD GAUSSIAN OVERLAP PARTICLES

The key result of this paper is the computation of the phase diagram of HPR particles and its comparison to the phase behavior of pears, as approximated by the PHGO model. Whereas PHGO particles were found to form complex phases (including smectic and gyroid), these phases are absent in the phase diagram of hard pears of revolution (HPR).

A. Phase behavior of pear hard Gaussian overlap (PHGO) particles

To highlight the sensitivity of the special collective behavior of PHGO pears in terms of particle shape, the phase diagram of the PHGO pear-shaped particle model, which has been obtained in Ref. 30, is revisited and put into perspective in the following. In Ref. 30, a complete phase diagram of PHGO particles with aspect ratio $k = 3$ is calculated (see also the recreated phase diagram in Fig. 3). Depending on the tapering parameter, the phase diagram can be separated into three regimes. Two parts, containing pears with high ($k_\theta < 2.3$) and intermediate tapering ($2.3 < k_\theta < 4.5$), are characterized by the formation of bilayer-phases, namely, the bilayer smectic and the gyroid configuration. The third fraction ($k_\theta > 4.5$) of the phase diagram involves nearly ellipsoidal particles that generate monolayer states such as nematic and monolayer smectic.

B. Phase behavior of hard pears of revolution (HPR)

The slight shape change of the pear particles is realized by changing the model to describe pear particle interactions from the PHGO to the HPR representation. The calculated phase diagram is based on *NVT* Monte Carlo simulations with $N = 400$ and $N = 1600$ monodisperse HPR particles interacting via a hard-core potential. The boundary conditions of the cuboidal simulation box are set as periodic in all three directions. The tapering parameter k_θ lies between 2.0 and 5.0, which corresponds to tapering angles between 28.1° and 11.4°. The MC translation step and the rotation step are initially set as $\Delta_{q,\text{max}} = 0.015\sigma_w$ and $\Delta_{u,\text{max}} = 0.015\sigma_w$,[40] respectively, but have been adjusted in an equilibration phase to maintain acceptance rates of roughly 50% for the displacement attempts.

Every simulation starts from an initially crystalline arrangement of particles at very low density ($\rho_g = 0.1$), which is then compressed to the global density $\rho_g = 0.44$, where all systems are obtained in the isotropic phase. Subsequently, the systems are slowly compressed further (see symbols in Fig. 3). For each data point of the sequence, the assembly is equilibrated for $2 \cdot 10^6$ MC steps and afterward analyzed for $1.8 \cdot 10^7$ step, where snapshots are taken after every 10 000th step. At very high densities $\rho_g = 0.63$, the mean squared displacement of the individual pears indicates the trapped particles. These particles hardly diffuse within the simulation box during simulation runs. This could be an indicator of a solid state. However, our simple Metropolis MC method is not sufficient to access this region reliably. Thus, solid phases are not drawn in the phase diagram. Afterward, expansion sequences are performed in an equivalent, but reverse, manner from each $\rho_g = 0.63$ state. The resultant phase diagram is shown in Fig. 3.

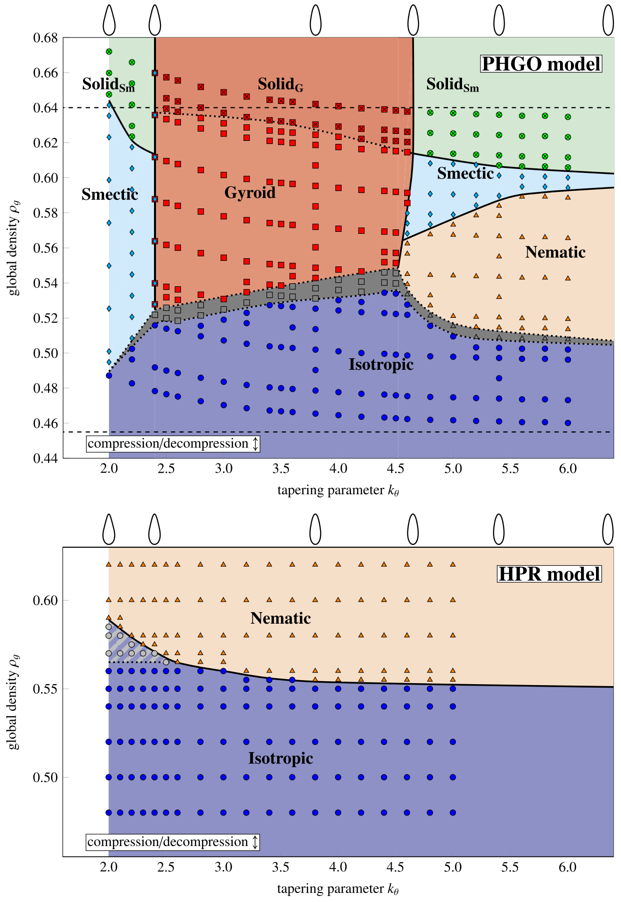

FIG. 3. (a) Phase diagram of hard PHGO pear-shaped particles with $k = 3.0$ obtained by compression (from isotropic) and decompression at fixed tapering parameter k_θ for systems of 3040 particles in a cubic simulation box. Gray regions between the isotropic and ordered phases indicate parameter values for which phase hysteresis is observed between compression and decompression sequences. The phase diagram is adopted from Ref. 30. (b) Phase diagram of hard HPR particles with $k = 3.0$ obtained by compression (from isotropic) and decompression at fixed tapering parameter k_θ for systems of 400 and 1600 particles in a cubic simulation box. Gray shaded regions indicate configurations that demonstrate a high degree of local orientational order and basic features, which could lead to bilayer formations according to their pair-correlation functions (see Fig. 8). However, this should not be seen as a separate phase from the isotropic state. The schematics above both graphs indicate the cross-sectional shape of the particles associated with each k_θ value.

Already at first sight, the HPR phase diagram differs starkly from the phase diagram of PHGO particles. It becomes apparent that the remarkable division into three different regimes in terms of shape is absent. Independent of tapering, all particles feature a similar phase behavior. For low densities, the particles adopt the expected isotropic phase. However, during the compression, the pear-shaped particles begin to globally align with the director of the system and eventually transition into a nematic state (see nematic order parameter in Fig. 4).

Also at direct visual comparison between the HPR and PHGO assemblies, the major distinctions become apparent (see the characteristic configurations pictured in Fig. 5). Next to the absence of gyroid phases and of the global alignment into one preferred directions, the HPR particles even lack of any indications of bilayer formation. Neither do they display interdigitated zig-zag patterns of anti-parallelly aligned pears nor is it feasible to detect layers or channel domains via distance clustering of their blunt ends for any given tapering parameter. By contrast, the influence of the tapering parameter k_θ is manifested in a shift of the transition density from the isotropic to the nematic phase. A greater head–tail asymmetry of the pear shape induces destabilization of the nematic order such that the transition occurs for larger densities. Also note that the hysteresis effects are marginal compared to those observed in the process of constructing Fig. 3. Consequently, the hysteresis is not drawn in this phase diagram. Moreover, the transition line coincides with previous observations of the isotropic–nematic transition for prolate ellipsoids with $k = 3$ and $k_\theta \to \infty$ ($\rho_{in} = 0.541$[2,41]). As the nematic phase arches over all values of k_θ, it becomes evident that HPR pears seem to be unable to form bilayer-structures via self-assembly.

The computational complexity of the overlap calculations for HPR implies that our results are based on fewer and shorter simulation runs. While the question of equilibration is a more persistent one than for PHGO, there are clear indications that the HPR behavior described above is a close representative of the equilibrium behavior: First, we have been unsuccessful in obtaining an equilibrated bilayer configuration even when the HPR systems are initially prepared as an artificial smectic or gyroid arrangement. Here, the pre-constructed structures destabilize and transition into nematic configurations upon equilibration. Second, during our simulations, the HPR pears hardly show any sign of precursors of bilayer formation. This, however, is a typical initial step in the isotropic phase of PHGO particles before entering the bilayer states.[30] The precursors appear as small randomly oriented clusters that are unjoined such that they do not form long-ranged structures. Only HPR particles within the gray area in Fig. 3 hint toward some of the characteristics of such bilayer precursors, which is discussed in more detail below.

IV. PAIR CORRELATION FUNCTIONS

Overall, we can draw the conclusion that the small differences between the PHGO and HPR models have major repercussions on the pears' ability to collectively form bilayer phases. To give an explanation for the drastic change in phase behavior, we investigate the local surrounding of the different phases by calculating the lateral $g^\perp$ and longitudinal $g^\parallel$ pair-correlation functions. As the local behavior is intimately linked with global phase behavior, this analysis, next to our studies on the depletion behavior of the two pear-shaped particle models in Paper II,[22] sheds light on the propensity of PHGO articles to form gyroid structures from a microscopic point of view. Here, we concentrate not only on the density distribution in lateral and longitudinal directions of the pears but also the polar and nematic weighted correlation functions. Before we apply these tools to the PHGO and HPR systems, however, we first describe the definition of $g(r)$ as a basis for our extended definition of $g^\perp$ and $g^\parallel$ below.

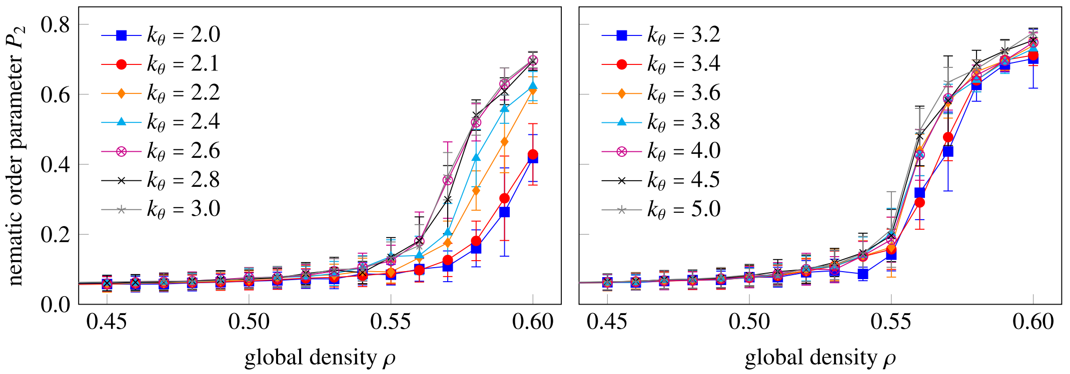

FIG. 4. The nematic order parameter P_2 during the compression of HPR particle systems with $N = 400$ for different tapering parameters k_θ.

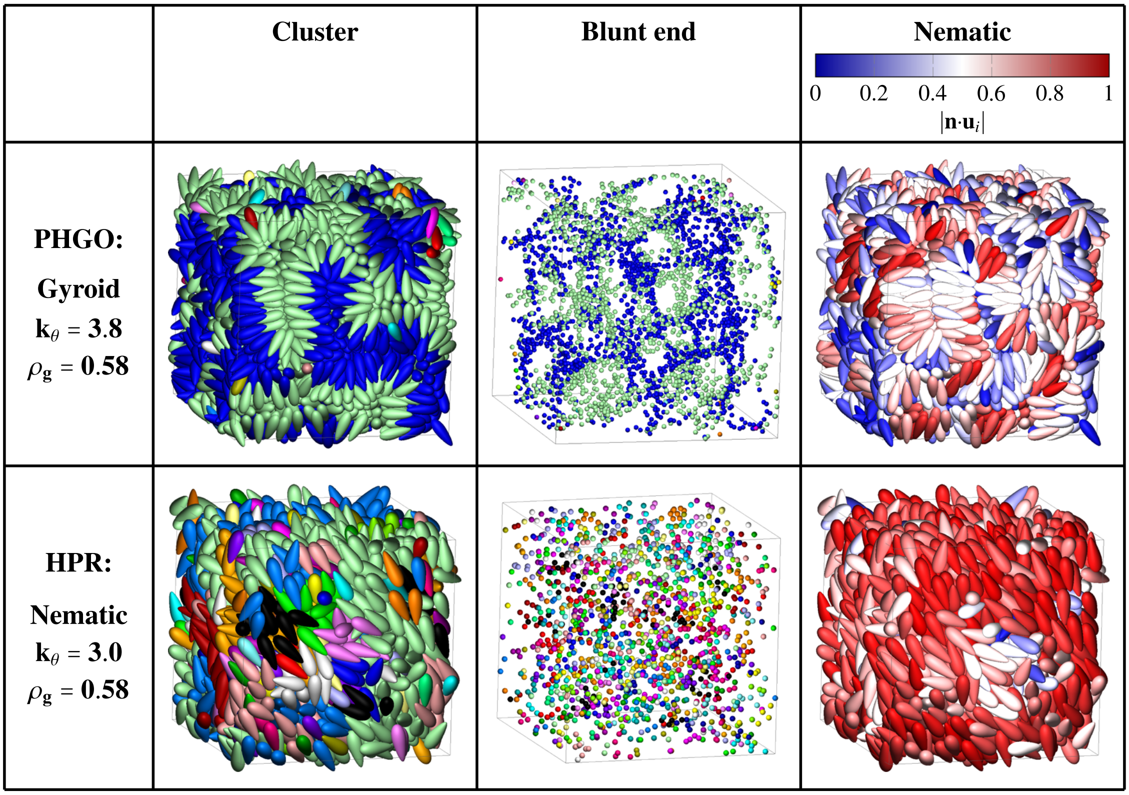

FIG. 5. Representative configurations of 3040 PHGO pear-shaped particles in the gyroid phase (first row: $k = 3$, $k_\theta = 3.8$, and $\rho_g = 0.60$) and 1600 HPR particles forming the nematic phase (second row: $k = 3$, $k_\theta = 3.0$, and $\rho_g = 0.58$). The structures are illustrated in the cluster representation (first column) and the blunt end representation (second column) where the colors indicate the cluster affiliation. In the third column, the particles are additionally colored according to their relative orientation to the director **n**.

A. Technical definition of pair correlation functions

One of the best established observables to characterize the translational order of particle systems is the *pair correlation function* $g(r)$, also known as the *radial distribution function*, which bears valuable information about the positional correlations between the particles. Based on the number density distribution function, the radial distribution function is written as

$$g(r) = \frac{1}{N\rho_N}\left\langle \sum_i \sum_{j\neq i} \delta(r - r_{ij}) \right\rangle, \tag{2}$$

with the global number density

$$\rho_N = \frac{N}{V}. \tag{3}$$

To calculate $g(r)$ numerically in our simulations, the mean number of particles $\delta N(r)$ found within a small distance interval $(r, r + \delta r)$ from another particle is determined by

$$\delta N(r) = \rho_N g(r) V_{\mathrm{shell}}(r), \tag{4}$$

with $V_{\mathrm{shell}}(r)$ being the volume of the thin spherical shell of thickness δr whose inner boundary is a sphere of radius r. By approximating $V_{\mathrm{shell}}(r) = V_{\mathrm{sph}}(r+\delta r) - V_{\mathrm{sph}}(r) \approx 4\pi r^2 \delta r + \mathcal{O}(\delta r^2)$ and rearranging Eq. (4), we obtain

$$g(r) = \frac{1}{\rho_N} \frac{\delta N(r)}{4\pi r^2 \delta r}. \tag{5}$$

This can be interpreted as a formula to generate the radial distribution function by a normalized histogram.[42] The concept is pictured in Fig. 6(a).

In the analysis of liquid crystals, it is often advantageous not to determine the radial distribution as described above, but to separate the distance between two molecules into a longitudinal and lateral part, particularly for smectic phases. Due to their anisotropic features, the order parallel to the director is different from the order perpendicular to the director. By calculating $g^{\parallel}(\mathbf{n} \cdot \; \mathbf{r})$ and $g^{\perp}(\sqrt{r^2 - (\mathbf{n} \cdot \mathbf{r})^2})$, the information is separated for the two directions. The former characterizes the smectic layering of the system, whereas the latter is a measure of translational order within the layers. However, this approach has the disadvantage that global orientational order is needed. Lipid systems adopting a bicontinuous surface geometry exhibit no overall global orientational order as they form pronouncedly curved bilayers. Nevertheless, locally neighboring lipids are clearly orientationally correlated such that a lateral and longitudinal distribution function on a local scale seems to be more effective. Thus, we replace the director with the orientation of the liquid crystal at the origin $\mathbf{u}_i$. In this way, we can guarantee to detect both curved bilayer ordering and smectic layering as $\mathbf{u}_i \approx \mathbf{n}$.[43] The longitudinal and lateral distances are defined by $r^{\parallel} = \mathbf{u}_i \cdot \mathbf{r}$ and $r^{\perp} = \sqrt{r^2 - r^{\parallel 2}}$, respectively.[44]

To compute the longitudinal distribution function $g^{\parallel}(r^{\parallel})$ and lateral distribution function $g^{\perp}(r^{\perp})$, we use a similar histogram approach like in Eq. (5). For simplifying the normalization of the histograms, they are calculated within a cylinder. This implies that only particles that lie within a cylinder with radius R_{cyl} and height H_{cyl} centered at the position of particle i are considered. The cylinder, furthermore, shares the same rotational symmetry axis as the very particle i [see Fig. 6(b)]. The dimensions of the encapsulating cylinder have to be chosen such that either only neighboring pears of the same bilayer $H_{\mathrm{cyl}} = k \cdot \sigma_w$ or one zig-zag motif $R_{\mathrm{cyl}} = 1.2\sigma_w$ is enclosed by the cylinder. The probability to find a particle at the longitudinal distance $r^{\parallel}$ within a circular disk of thickness $\delta r^{\parallel}$ and volume $V_{\mathrm{disk}} = \pi R_{\mathrm{cyl}}^2 \delta r^{\parallel}$ bounded by the cylinder is given by

$$g^{\parallel}(r^{\parallel}) = \frac{1}{\rho_N} \frac{\delta N^{\parallel}(r^{\parallel})}{\pi R_{\mathrm{cyl}}^2 \delta r^{\parallel}}, \tag{6}$$

where $\delta N^{\parallel}(r^{\parallel})$ is the mean number of particles within the disk. Analogously, the probability to find a particle at the lateral distance $r^{\perp}$ within a cylindrical shell of thickness $\delta r^{\perp}$ and volume $V_{\mathrm{disk}} \approx 2\pi r \delta r^{\parallel} H_{\mathrm{cyl}}$ is defined as

$$g^{\perp}(r^{\perp}) = \frac{1}{\rho_N} \frac{\delta N^{\perp}(r^{\perp})}{2\pi H_{\mathrm{cyl}} r^{\perp} \delta r^{\perp}}. \tag{7}$$

Here, $\delta N^{\perp}(r^{\perp})$ is the mean number of particles within the cylindrical shell. The notion of both distribution functions is depicted in Figs. 6(b) and 6(c).

The different distribution functions provide the possibility to study the local orientational ordering in a much more detailed way as well. Here, the number density in Eq. (2) can be weighted by a factor, which includes the relative orientations of the pear particles. With this take on $g(r)$, we can define a polar radial distribution function g_{P1} weighted by the first Legendre polynomial $P_1(\mathbf{u}_i \cdot \mathbf{u}_j) = \cos(\mathbf{u}_i \cdot \mathbf{u}_j)$,

$$g_{P_1}(r) = \frac{1}{N \delta N(r)} \left\langle \sum_i \sum_{j \neq i} \cos(\mathbf{u}_i \cdot \mathbf{u}_j) \delta(r - r_{ij}) \right\rangle. \tag{8}$$

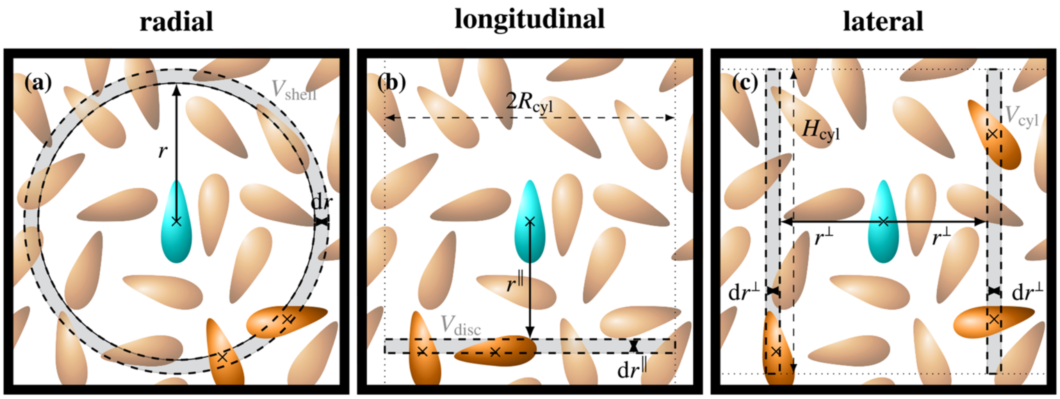

FIG. 6. Schematics of the radial (a), longitudinal (b), and lateral distribution function (c). These figures show cross sections through the sampling space. The gray areas represent shells, which bin the space around the center pear-shaped particle and are used to create the corresponding histogram. The shells are spherical (a), diskal (b), and cylindrical (c).

For the nematic radial distribution function g_{P2}, the second Legendre polynomial $P_2(\mathbf{u}_i{\cdot}\mathbf{u}_j) = \frac{1}{2}(3\cos^2(\mathbf{u}_i \cdot \mathbf{u}_j) - 1)$ is used as a weighting factor such that

$$g_{P_2}(r) = \frac{1}{N\delta N(r)}\left\langle \sum_i \sum_{j \neq i} \frac{1}{2}(3\cos^2(\mathbf{u}_i \cdot \mathbf{u}_j) - 1)\delta(r - r_{ij}) \right\rangle. \quad (9)$$

Both the polar and nematic distribution functions are scaled by the mean number of particles at distance r to easier relate the values to polar and nematic order parameters. This means that $g_{P_1}(r)$ and $g_{P_2}(r)$ determine how strongly two particles separated by a distance r are orientationally correlated.[45] In a similar vein also, lateral and longitudinal variants of the distributions are defined.

B. Pair correlation functions of PHGO systems

The lateral and longitudinal pair correlation functions are first applied to various PHGO systems, which represents the different phases in the phase diagram shown in Fig. 3. The local properties to form bilayers have a clear signature in the form of the different longitudinal pair-correlation functions $g^{\parallel}(z)$ of PHGO particles (see Fig. 7, left). In the case of the smectic bilayer phase, all three plots [Figs. 7(a)–7(c)] indicate multiple distinct peaks, suggesting both long ranged transitional, polar, and nematic order in the longitudinal direction and a piling of multiple sheets of pear-shaped particles. Moreover, the bifurcation of peaks in Fig. 7(a), for instance, the pair of peaks indicated by ■ and ★, implies an organization into stacks of interdigitated bilayers rather than monolayers. Here, the arrangement into parallel leaflets (■, ♦, ▼), where the polar order parameter P_1 locally exhibits positive values, and antiparallel leaflets of the bilayers (★, ▲), where P_1 changes sign, can be identified. This propensity to obtain the local polar order is also observed in pear-sphere-mixtures dominated by small hard spheres, where the PHGO particles align due to depletion attractions (see Paper II[22]). The leaflets are also affirmed by the $g^{\parallel}_{P_2}(z)$ profile of this phase in the form of small dips at each maximum. The lateral pair-correlations also indicate the smectic bilayer phase (see Fig. 7, right). First, the weighted functions show that the particles are aligned for large lateral distances, suggesting that the layers are flat. Second, a small peak (■) before the main peak is observable in Figs. 7(d) and 7(f), which can be assigned to the immediate antiparallel and parallel neighbors of the reference pears in the same bilayer, respectively.

Analogously, the pair correlation functions belonging to gyroid forming PHGO particle systems prove that single particles arrange within interdigitating curved bilayers. The characteristics of the distance distributions are locally similar to those observed in the flat bilayer-smectic phase of strongly tapered pears. The bifurcation of peak (a) and the clear bump at the location of the secondary minor maximum for small $r^{\perp}$ in the bilayer smectic phase (d) coincide with the architecture of interdigitated bilayers. Yet, both of these plots also point to considerable differences on a larger length scale. The correlations are less distinct and diminish faster in the longitudinal and lateral directions, which can be explained by the inherent curvature of the minimal surface structure. The influence of the warped bilayers is reflected even more in the characteristics of the weighted pair correlation functions. First, the polar order vanishes in (b) and (e) for large distances and is less periodic. Second the nematic order in (c) oscillates around 0 and, like the plot in (f), eventually approaches this very value for $r^{\parallel} \rightarrow \infty$. This means that the stacks of bilayers do not lie parallel to each other anymore and also that largely separated particles within the same leaflet are likely to be differently oriented.

In addition, the pair-correlation functions of the nematic and monolayer smectic give valuable information about the importance of the mentioned signatures of the different $g(r)$s for bilayer assembly. Although both translational and orientational orders are still present, the correlations are weaker than for bilayer arrangements. Furthermore, the plots not only differ quantitatively but also qualitatively. On the one hand, the division into two maxima per peak for $g^{\parallel}(r^{\parallel})$ in Fig. 7(a) vanishes. On the other hand, the small secondary peak, which was contributed to the opposite leaflet of a bilayer, also disappears for small $r^{\perp}$ in $g^{\perp}(r^{\perp})$ [see ■ in Fig. 7(d)]. Both of these phenomena can be explained by the lack of inversion asymmetry. In this regime, the particles are not tapered enough to interdigitate into a neighboring sheet and rather form a separate monolayer. Moreover, the weak taper causes the polarity within a sheet to be less pronounced (indicated by the overall small peaks in the P_1 profiles) as in the bilayer smectic phase such that antiparallel particles can be found within the same leaflet more often [high peak at ★ in Fig. 7(d)]. This also causes the profile of the nematic and monolayer smectic phases in Fig. 7(c) to be more homogeneous at a high mean nematic value.

C. Pair correlation functions of HPR systems

Based on these observations gained from the PHGO particles, we can deduce the lack of bilayer phases in the HPR phase diagram by an analysis of these phases' local behavior. The profiles of the pair correlation functions in the nematic and the isotropic phase close to the transition line (see Fig. 8) exhibit both similarities and differences to the liquid crystal phases of the PHGO pear systems in Fig. 7. The lateral pair-correlation functions $g^{\perp}(r^{\perp})$ of the nematic phases of both pear models, for example, produce similar plots, also comparable to the monolayer smectic of the PHGO model. The characteristic minor peak before the first major peak [see □ in Fig. 8(d)], however, which have been attributed to interdigitating bilayer arrangements, is not present. Only for pears close to $k_\theta = 2.0$, this peak is implied by a bump. The profiles of $g^{\perp}_{P_2}(r^{\perp})$ are also akin (even if the alignment is not as strong) to the not-bilayer forming liquid crystal phases of the weakly tapered PHGO pears. The most significant difference in terms of lateral correlation, however, is in the polarity of the neighboring particles in Fig. 8(e). For HPR pears, the nearest neighbors show basically no preference of parallel or anti-parallel orientation. The high degree of local polar order for PHGO pears is at best vaguely reflected and largest for $k_\theta < 2.5$.

The plots of the longitudinal pair correlations $g^{\parallel}(r^{\parallel})$ shown in Fig. 8 (left), however, also indicate why the particles are not arranged within a bilayer formation and rather create nematic phases. The most noticeable one is the missing peak [□ in Fig. 8(a)] at $r^{\parallel} = 0$ in the nematic and monolayer smectic phases. This signifies that this particular correlation is crucial for the formation of bilayer phases as it corresponds to particles sitting side by side to another. All other peaks (☆, △, ◊) can be attributed to their counterparts in the $g^{\parallel}(r^{\parallel})$-signature of the nematic/smectic phases of the PHGO pears

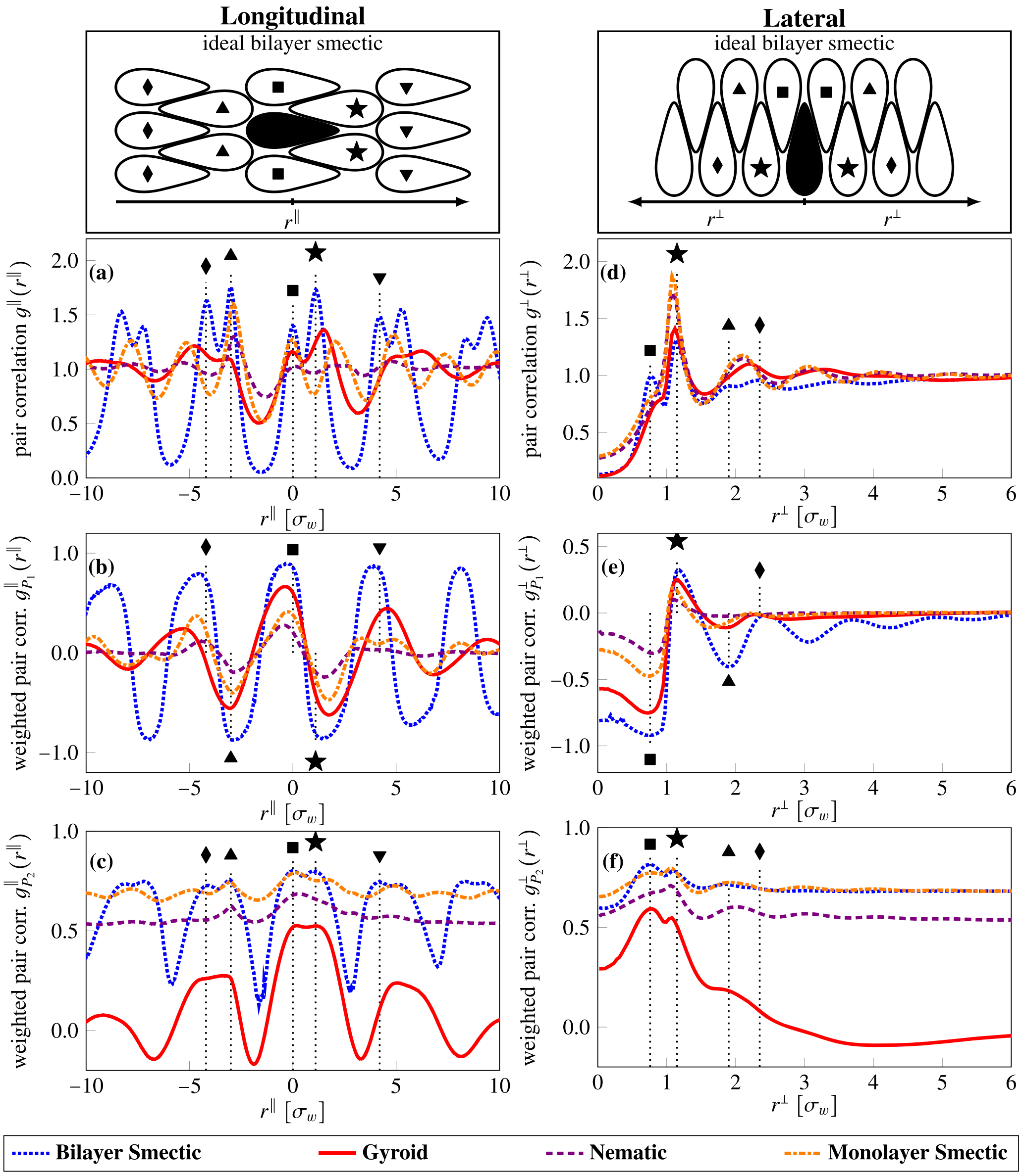

FIG. 7. The longitudinal pair-correlation function $g^{\parallel}(r^{\parallel})$ [(a)–(c)] and the lateral pair-correlation function $g^{\perp}(r^{\perp})$ [(d)–(f)] of the smectic bilayer ($k_\theta = 2.2$, $\rho_g = 0.57$), the gyroid ($k_\theta = 3.8$, $\rho_g = 0.56$), the nematic ($k_\theta = 5.4$, $\rho_g = 0.56$), and the smectic monolayer phase ($k_\theta = 5.4$, $\rho_g = 0.585$). The pair-correlation functions are additionally weighted by the polar order parameter P_1 (second row) and the nematic order parameter P_2 (third row).

but seem to be closer together. Furthermore, the weighted functions indicate that the reference pears barely influence the polar preference of their neighbor's orientation, not even longitudinal direction. On a similar note, the local nematic order indicated by the minor peaks, even though obviously present, is not as pronounced and long ranged in this model, not to mention the double peaks, which can be observed for all liquid crystal phases in Fig. 7, but are not noticeable here.

Despite these distinctions, similarities can be determined as well. For once, the pears tend to aggregate preferentially at the blunt ends ($r^{\parallel} < 0$) rather than the pointy ends ($r^{\parallel} > 0$) of other particles. This leads to the assumption that, in principle, the mechanism, which brings the pears together with their blunt ends to form clusters, also exists in the HPR model. Unfortunately, the impact of this mechanism is not strong enough to indeed induce the self-assembly of bigger clusters (see cluster representation in

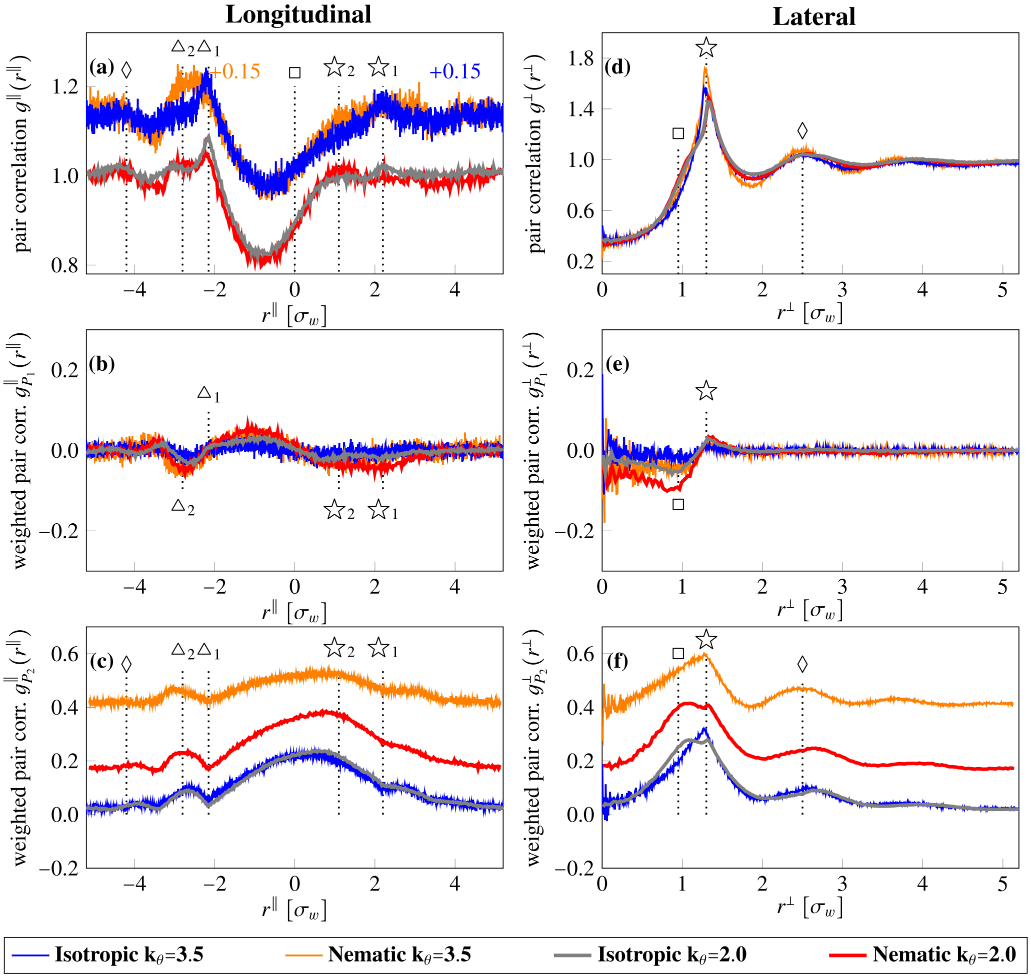

FIG. 8. The longitudinal pair-correlation function $g^{\parallel}(r^{\parallel})$ [(a)–(c)] and the lateral pair-correlation function $g^{\perp}(r^{\perp})$ [(d)–(f)] of the isotropic ($k_\theta = 2.0$:$\rho_g = 0.58$ and $k_\theta = 3.5$:$\rho_g = 0.55$) and nematic ($k_\theta = 2.0$:$\rho_g = 0.6$ and $k_\theta = 3.5$:$\rho_g = 0.58$) in systems of $N = 400$ HPR particles. The pair-correlation functions are additionally weighted by the polar order parameter P_1 (second row) and the nematic order parameter P_2 (third row).

Fig. 5). More intriguing, however, is the observation that for highly tapered particles $k_\theta < 2.5$, the peaks of $g^{\parallel}(r^{\parallel})$ (☆$_1$, ☆$_2$, and △$_1$, △$_2$) and $g^{\perp}_{P_2}(r^{\perp})$ (□ and ☆) widen considerably or even split into two. This can be already observed in the isotropic phase close to the phase transition. The area within the system that demonstrates these indications of bifurcation is shaded in the phase diagram. Thus, some of the basic conditions for bilayer formation are also met at least for highly tapered HPR particles. Nevertheless, without additional features to the contact function, these effects are too weak to produce a more complex phase behavior than nematic.

In this paper, we focused exclusively on pear-shaped particles with a specific aspect ratio of $k = 3$. While possible, it is unlikely that a different choice of k for the HPR would have yielded a different phase behavior for the following reasons. First, by increasing the aspect ratio, the maximum adjustable taper of convex pear-shaped particle decreases. As we have shown that higher taper implies higher local order, we can rule out the existence of the gyroid phase in HPR systems for $k \geq 3$. Second, less elongated hard particles usually lose their ability to create global orientational order (rule of thumb $k < 2.75$[1,2]) and form isotropic configurations instead. Therefore, the window of aspect ratios, which comes into consideration, seems too small to increase the local polar order in Figs. 8(b) and 8(e) to values, which are needed to achieve bilayering comparable to PHGO systems.

V. CONCLUSION AND OUTLOOK

The overarching theme of this paper concerned the stability of the gyroid phase with respect to particle shape, particularly the difference in phase behavior between HPR and PHGO particles. Hence, it fits closely with the broader topic of how self-assembly (in particular in hard core systems) is sensitive to the details of the particle shape.[4–9,23–28] In particular, we compared two hard pear-shaped particle models on the microscopic scale and their abilities to form the double gyroid spontaneously globally. One is the pear hard Gaussian overlap (PHGO) particle, which closely approximates a pear-shape but also features self-non-additive properties. The other model represents the exact pear shape perfectly and is called the hard pear of revolution (HPR) model.

Therefore, we revisited the phase behavior of PHGO particles and additionally generated a phase diagram based on particles interacting according to strict hard-core HPR interactions. In contrast to the rich phase diagram of PHGO particles containing nematic and monolayer smectic, but also both bilayer smectic and bilayer gyroid structures, we observed in the HPR systems only a rudimentary phase behavior. More precisely, the HPR systems form nematic liquid crystal phases for all particle shapes analyzed (i.e., all k_θ), where more highly tapered particles visibly destabilize the nematic order and push the transition to higher densities. However, both the gyroid and bilayer smectic phases, characteristic for the phase behavior of PHGO particles, vanish.

According to these observations, the small differences in the contact function between the PHGO and HPR model, which can easily, but mistakenly, be considered negligible, have a major impact on the self-assembly of pear-shaped particles. Even though most features of a pear (such as aspect ratio and tapering parameter) are present in both models, the PHGO particles have to offer additional morphological properties to which the stability of the gyroid phase is ascribed. This is also supported by the fact that only the nematic phase is obtained, which has also been found for PHGO pears with small tapering angles. In this regime of large k_θ, the two pear models differ the least in terms of contact functions. Hence, their collective behaviors are very similar. All these results lead to the assumption that the formation of bilayer structures, including the double gyroid phase, is due to the special orientation dependency of the PHGO contact function. In particular, the self-non-additive features in reference to the pear shape seem to magnify the spontaneous placement of pears side to side. This mechanism would naturally lead to sheets, which then interdigitate due to the pointy ends of the individual particles. Not only the HPR model and our depletion studies in Paper II[22] hint toward the validity of this hypothesis, also other models that lack self-non-additive features but look similar to pears are known to fail assembling into the bilayer configuration. Neither hard multisphere particles, such as snowman[46] or asymmetric dumbbell particles,[47] nor conical colloids[48] show any propensity to form the gyroid.

Despite the differences in phase behavior, the self-assembly of some HPR particles with small k_θ close to the phase transition also demonstrates interesting properties, which were attributed as necessary precursors to the formation of bilayers. Therefore, it is conceivable that the HPR particles might be able to form similar phases such as the PHGO pears, if we, for instance, add suitable changes to the pear-shape or introduce non-additivity to the HPR contact function. These particle modifications also have the potential to be utilized as a regulating mechanism to control the coupling strength between the blunt ends. This might allow us to create a model for pear-shaped particles, based on those indicated by the gray-striped area in Fig. 3, with an intermediate degree of blunt end aggregation. A first attempt to conceptualize such a pear-shaped particle model is made in Paper II.[22] In general, these particles could potentially form phases with a short-range order, sufficient to display a bicontinuous network, but also display with disorder over larger length scales. These disordered cubic phases are known as L_3 sponge phases[49] and are formed typically in lipid-water mixtures by swelling the cubic phases due to the presence of additives.[50–58]

The formation of gyroid structures in pear-shaped PHGO particle systems remains a fascinating finding. This is particularly so because of the mechanism of creating a propensity for the formation of interdigitated "smectic-like" warped bilayers. While particle shape clearly plays a crucial role in this, this paper has highlighted the subtleties, namely, that the effect vanishes for the additive hard pear HPR model. This, in turn, brings us back to the opening statement that the particle shape is a double-edged sword. Surely, the "coarse" (or first order) characterization of the particles as pear-shaped is critical for the process. Yet, pear-shaped appearance is not sufficient to ensure the effect that occurs, as the lack of the gyroid in the HPR phase diagram demonstrates. It appears that first-order shape characteristics are a necessary condition for some structure phase formation but not sufficient criteria.

As a closing note, we want to mention here that it is difficult to judge which of the two pear models represents the interactions of pear-shaped particles, which might be synthesized in the future, better. For example, it is well established that colloids in experimental systems are never truly hard and the interparticle potential always inherits some degree of softness.[59–62] Therefore, the potentials we used here—both the PHGO *and* HPR potentials—have to be considered as approximations of a real pear-shaped colloid. This becomes even more important as recent studies show that the introduction of already a small degree of softness can influence the stability of crystalline phases.[63] Additionally, pear-shaped particles have not been synthesized yet. In principle, many different strategies to produce nanoparticles with aspherical shapes have been developed via methods such as templates,[64–66] particle swelling and phase separation,[67–69] seeded emulsion polymerization,[70–73] controlled deformation of spherical colloids,[74–76] particle confinement,[77] or lithography.[78–80] However, many of these techniques are still limited in either their customizability of the particle shape, rely on colloids as a basic shape, or cannot be mass-produced easily. Furthermore, it is difficult to draw practical knowledge from the formation of other bilayer forming systems prominent in nature and chemistry. It has been shown earlier that the collective mechanism of PHGO particles to form bilayers via interdigitation is fundamentally different from the one observed in amphiphilic lipidic or polymeric systems and based on the shape change of individual molecules.[30] All these difficulties seem to be exacerbated by the big contrast of the two phase diagrams in Fig. 3, which highlights that in both experiments and simulations even small nuances of the interaction profiles of molecules have to be taken into account to predict the right phase behavior. In addition, the composite sphere method, where complexly shaped particles are modeled from multiple sphere constituents, is known to face issues with inaccuracies due to the degraded smoothness of the particle surface.[81–83]

ACKNOWLEDGMENTS

We thank Universities Australia and the German Academic Exchange Service (DAAD) for funds through a collaboration funding scheme and through the grant "Absorption and confinement of complex fluids." We also thank the DFG (Grant No. ME1361/11-2) and the research group "Geometry and Physics of Spatial Random Systems" (GPSRS) for funding. We gratefully acknowledge Klaus Mecke's support and advice in useful discussions. P.W.A.S. acknowledges a Murdoch University Postgraduate Research Scholarship. G.E.S.-T. is grateful to the Food Science Department at the University of Copenhagen and the Physical Chemistry group at Lund University for their hospitality and to Copenhagen University, the Camurus Lipid Research Foundation, and the Danish National Bank for enabling a sabbatical stay in Denmark and Sweden.

DATA AVAILABILITY

The data that support the findings of this study are available within this article. Dataset lists are available from the corresponding authors upon reasonable request.

REFERENCES

[1] J. A. C. Veerman and D. Frenkel, "Phase diagram of a system of hard spherocylinders by computer simulation," Phys. Rev. A **41**(6), 3237 (1990).

[2] D. Frenkel, B. M. Mulder, and J. P. McTague, "Phase diagram of a system of hard ellipsoids," Phys. Rev. Lett. **52**(4), 287 (1984).

[3] A. Haji-Akbari, M. Engel, and S. C. Glotzer, "Phase diagram of hard tetrahedra," J. Chem. Phys. **135**(19), 194101 (2011).

[4] R. Ni, A. P. Gantapara, J. de Graaf, R. van Roij, and M. Dijkstra, "Phase diagram of colloidal hard superballs: From cubes via spheres to octahedra," Soft Matter **8**(34), 8826–8834 (2012).

[5] P. F. Damasceno, M. Engel, and S. C. Glotzer, "Crystalline assemblies and densest packings of a family of truncated tetrahedra and the role of directional entropic forces," ACS Nano **6**(1), 609–614 (2011).

[6] P. F. Damasceno, M. Engel, and S. C. Glotzer, "Predictive self-assembly of polyhedra into complex structures," Science **337**(6093), 453–457 (2012).

[7] A. P. Gantapara, J. de Graaf, R. van Roij, and M. Dijkstra, "Phase diagram and structural diversity of a family of truncated cubes: Degenerate close-packed structures and vacancy-rich states," Phys. Rev. Lett. **111**(1), 015501 (2013).

[8] C. X. Du, G. van Anders, R. S. Newman, and S. C. Glotzer, "Shape-driven solid–solid transitions in colloids," Proc. Natl. Acad. Sci. U. S. A. **114**(20), E3892–E3899 (2017).

[9] D. Klotsa, E. R. Chen, M. Engel, and S. C. Glotzer, "Intermediate crystalline structures of colloids in shape space," Soft Matter **14**(43), 8692–8697 (2018).

[10] P. Bolhuis and D. Frenkel, "Tracing the phase boundaries of hard spherocylinders," J. Chem. Phys. **106**(2), 666–687 (1997).

[11] B. S. John, C. Juhlin, and F. A. Escobedo, "Phase behavior of colloidal hard perfect tetragonal parallelepipeds," J. Chem. Phys. **128**(4), 044909 (2008).

[12] M. Marechal, S. Dussi, and M. Dijkstra, "Density functional theory and simulations of colloidal triangular prisms," J. Chem. Phys. **146**(12), 124905 (2017).

[13] The standard deviation of the diameter distribution has to be $\sigma_d \gtrapprox 0.08\bar{d}$ with the mean diameter $\bar{d}$.

[14] P. Bartlett and P. B. Warren, "Reentrant melting in polydispersed hard spheres," Phys. Rev. Lett. **82**(9), 1979 (1999).

[15] M. Adams, Z. Dogic, S. L. Keller, and S. Fraden, "Entropically driven microphase transitions in mixtures of colloidal rods and spheres," Nature **393**(6683), 349 (1998).

[16] M. A. Bates and D. Frenkel, "Phase behavior of model mixtures of colloidal disks and polymers," Phys. Rev. E **62**(4), 5225 (2000).

[17] Z. Dogic, K. R. Purdy, E. Grelet, M. Adams, and S. Fraden, "Isotropic-nematic phase transition in suspensions of filamentous virus and the neutral polymer dextran," Phys. Rev. E **69**(5), 051702 (2004).

[18] S. Belli, M. Dijkstra, and R. van Roij, "Depletion-induced biaxial nematic states of boardlike particles," J. Phys.: Condens. Matter **24**(28), 284128 (2012).

[19] R. Aliabadi, M. Moradi, and S. Varga, "Tracking three-phase coexistences in binary mixtures of hard plates and spheres," J. Chem. Phys. **144**(7), 074902 (2016).

[20] Á. G. García, J. Opdam, and R. Tuinier, "Phase behaviour of colloidal superballs mixed with non-adsorbing polymers," Eur. Phys. J. E **41**(9), 110 (2018).

[21] Á. G. García, R. Tuinier, J. V. Maring, J. Opdam, H. H. Wensink, and H. N. W. Lekkerkerker, "Depletion-driven four-phase coexistences in discotic systems," Mol. Phys. **116**(21-22), 2757–2772 (2018).

[22] P. W. A. Schönhöfer, M. Marechal, D. J. Cleaver, and G. E. Schröder-Turk, "Self-assembly and entropic effects in pear-shaped colloid systems: II. Depletion attraction of pear-shaped particles in a hard sphere solvent," J. Chem. Phys. **153**, 034904 (2020).

[23] R. D. Batten, F. H. Stillinger, and S. Torquato, "Phase behavior of colloidal superballs: Shape interpolation from spheres to cubes," Phys. Rev. E **81**(6), 061105 (2010).

[24] Y. Zhang, F. Lu, D. van der Lelie, and O. Gang, "Continuous phase transformation in nanocube assemblies," Phys. Rev. Lett. **107**(13), 135701 (2011).

[25] L. Rossi, V. Soni, D. J. Ashton, D. J. Pine, A. P. Philipse, P. M. Chaikin, M. Dijkstra, S. Sacanna, and W. T. M. Irvine, "Shape-sensitive crystallization in colloidal superball fluids," Proc. Natl. Acad. Sci. U. S. A. **112**(17), 5286–5290 (2015).

[26] S. Dussi and M. Dijkstra, "Entropy-driven formation of chiral nematic phases by computer simulations," Nat. Commun. **7**, 11175 (2016).

[27] M. Marechal and M. Dijkstra, "Phase behavior and structure of colloidal bowl-shaped particles: Simulations," Phys. Rev. E **82**(3), 031405 (2010).

[28] D. Wan, C. X. Du, G. van Anders, and S. C. Glotzer, "FCC-to-BCC phase transitions in convex and concave hard particle systems," J. Phys. Chem. B **123**(42), 9038–9043 (2019).

[29] L. J. Ellison, D. J. Michel, F. Barmes, and D. J. Cleaver, "Entropy-driven formation of the gyroid cubic phase," Phys. Rev. Lett. **97**(23), 237801 (2006).

[30] P. W. A. Schönhöfer, L. J. Ellison, M. Marechal, D. J. Cleaver, and G. E. Schröder-Turk, "Purely entropic self-assembly of the bicontinuous $Ia\bar{3}d$ gyroid phase in equilibrium hard-pear systems," Interface Focus **7**, 20160161 (2017).

[31] P. W. A. Schönhöfer, D. J. Cleaver, and G. E. Schröder-Turk, "Double diamond phase in pear-shaped nanoparticle systems with hard sphere solvent," J. Phys. D: Appl. Phys. **51**(46), 464003 (2018).

[32] F. Barmes, M. Ricci, C. Zannoni, and D. J. Cleaver, "Computer simulations of hard pear-shaped particles," Phys. Rev. E **68**, 021708 (2003).

[33] A. Perera, "Fluids of hard natural and Gaussian ellipsoids: A comparative study by integral equation theories," J. Chem. Phys. **129**(19), 194504 (2008).

[34] P. Ballone, G. Pastore, G. Galli, and D. Gazzillo, "Additive and non-additive hard sphere mixtures: Monte Carlo simulation and integral equation results," Mol. Phys. **59**(2), 275–290 (1986).

[35] E. Lomba, M. Alvarez, L. L. Lee, and N. G. Almarza, "Phase stability of binary non-additive hard-sphere mixtures: A self-consistent integral equation study," J. Chem. Phys. **104**(11), 4180–4188 (1996).

[36] R. Roth and R. Evans, "The depletion potential in non-additive hard-sphere mixtures," Europhys. Lett. **53**(2), 271 (2001).

[37] P. Hopkins and M. Schmidt, "Binary non-additive hard sphere mixtures: Fluid demixing, asymptotic decay of correlations and free fluid interfaces," J. Phys.: Condens. Matter **22**(32), 325108 (2010).

[38] K. Zhang, M. Fan, Y. Liu, J. Schroers, M. D. Shattuck, and C. S. O'Hern, "Beyond packing of hard spheres: The effects of core softness, non-additivity, intermediate-range repulsion, and many-body interactions on the glass-forming ability of bulk metallic glasses," J. Chem. Phys. **143**(18), 184502 (2015).

[39] Additional overlap rules (like adding non-additive features to the blunt ends) are required to imitate the interactions between PHGO particles with physical hard shapes.

[40] The parameter σ_w indicates the width of the pear-shaped particles.

[41] G. Odriozola, "Revisiting the phase diagram of hard ellipsoids," J. Chem. Phys. **136**(13), 134505 (2012).

[42] Note that the "normalization" factor in this case indicates that $g(r)$ converges toward 1 for large distances: $\lim_{r\to\infty} g(r) = 1$.

[43] This only applies to the smectic-A phase. For other smectic phases, it is still more convenient to use the director as a reference.

[44] Note here, that $r^{\parallel}$ can become negative. For pear-shaped particles, positive longitudinal distances correspond to a distance in the direction of the thin narrow end, while negative distances have to be assigned to particles, which are placed in the direction of the thick blunt end.

[45] Note that the functions do not contain information about the likeliness of such configurations occurring.

[46] M. Dennison, K. Milinković, and M. Dijkstra, "Phase diagram of hard snowman-shaped particles," J. Chem. Phys. **137**(4), 044507 (2012).

[47] K. Milinković, M. Dennison, and M. Dijkstra, "Phase diagram of hard asymmetric dumbbell particles," Phys. Rev. E **87**(3), 032128 (2013).

[48] J. van den Hoven, "Phase behaviour of conical colloids," M.Sc. thesis, Universiteit Utrecht, 2016.

[49] D. Anderson, H. Wennerstroem, and U. Olsson, "Isotropic bicontinuous solutions in surfactant-solvent systems: The L3 phase," J. Phys. Chem. **93**(10), 4243–4253 (1989).

[50] S. Engström, K. Alfons, M. Rasmusson, and H. Ljusberg-Wahren, "Solvent-induced sponge (L_3) phases in the solvent-monoolein-water system," Prog. Colloid Polym. Sci. **108**, 93–98 (1998).

[51] H. Evertsson, P. Stilbs, G. Lindblom, and S. Engström, "NMR self diffusion measurements of the monooleoylglycerol/poly ethylene glycol/water L_3 phase," Colloids Surf., B **26**(1-2), 21–29 (2002).

[52] V. Cherezov, J. Clogston, M. Z. Papiz, and M. Caffrey, "Room to move: Crystallizing membrane proteins in swollen lipidic mesophases," J. Mol. Biol. **357**(5), 1605–1618 (2006).

[53] S. Abe and H. Takahashi, "A comparative study of the effects of dimethylsulfoxide and glycerol on the bicontinuous cubic structure of hydrated monoolein and its phase behavior," Chem. Phys. Lipids **147**(2), 59–68 (2007).

[54] A. B. Wöhri, L. C. Johansson, P. Wadsten-Hindrichsen, W. Y. Wahlgren, G. Fischer, R. Horsefield, G. Katona, M. Nyblom, F. Öberg, G. Young, R. J. Cogdell, N. J. Fraser, S. Engström, and R. Neutze, "A lipidic-sponge phase screen for membrane protein crystallization," Structure **16**(7), 1003–1009 (2008).

[55] T. Landh, "Phase behavior in the system pine needle oil monoglycerides-poloxamer 407-water at 20 degree," J. Phys. Chem. **98**(34), 8453–8467 (1994).

[56] J. Barauskas, A. Misiunas, T. Gunnarsson, F. Tiberg, and M. Johnsson, ""sponge" nanoparticle dispersions in aqueous mixtures of diglycerol monooleate, glycerol dioleate, and polysorbate 80," Langmuir **22**(14), 6328–6334 (2006).

[57] R. Iñiguez-Palomares, H. Acuña-Campa, and A. Maldonado, "Effect of polymer on the elasticity of surfactant membranes: A light scattering study," Phys. Rev. E **84**(1), 011604 (2011).

[58] M. Valldeperas, M. Wiśniewska, M. Ram-On, E. Kesselman, D. Danino, T. Nylander, and J. Barauskas, "Sponge phases and nanoparticle dispersions in aqueous mixtures of mono- and diglycerides," Langmuir **32**(34), 8650–8659 (2016).

[59] P. N. Pusey and W. Van Megen, "Phase behaviour of concentrated suspensions of nearly hard colloidal spheres," Nature **320**(6060), 340 (1986).

[60] P. N. Pusey and W. van Megen, in *Physics of Complex and Supramolecular Fluids*, edited by S. A. Safran and N. A. Clark (Wiley, New York, 1987), pp. 673–698.

[61] W. C. K. Poon, E. R. Weeks, and C. P. Royall, "On measuring colloidal volume fractions," Soft Matter **8**(1), 21–30 (2012).

[62] C. P. Royall, W. C. K. Poon, and E. R. Weeks, "In search of colloidal hard spheres," Soft Matter **9**(1), 17–27 (2013).

[63] R. A. LaCour, C. S. Adorf, J. Dshemuchadse, and S. C. Glotzer, "Influence of softness on the stability of binary colloidal crystals," ACS Nano **13**(12), 13829–13842 (2019).

[64] J. P. Rolland, B. W. Maynor, L. E. Euliss, A. E. Exner, G. M. Denison, and J. M. DeSimone, "Direct fabrication and harvesting of monodisperse, shape-specific nanobiomaterials," J. Am. Chem. Soc. **127**(28), 10096–10100 (2005).

[65] S. H. Lee, S. J. Gerbode, B. S. John, A. K. Wolfgang, F. A. Escobedo, I. Cohen, and C. M. Liddell, "Synthesis and assembly of nonspherical hollow silica colloids under confinement," J. Mater. Chem. **18**(41), 4912–4916 (2008).

[66] L. Chen, H. Z. An, and P. S. Doyle, "Synthesis of nonspherical microcapsules through controlled polyelectrolyte coating of hydrogel templates," Langmuir **31**(33), 9228–9235 (2015).

[67] J. Kim, R. J. Larsen, and D. A. Weitz, "Synthesis of nonspherical colloidal particles with anisotropic properties," J. Am. Chem. Soc. **128**(44), 14374–14377 (2006).

[68] W. K. Kegel, D. Breed, M. Elsesser, and D. J. Pine, "Formation of anisotropic polymer colloids by disparate relaxation times," Langmuir **22**(17), 7135–7136 (2006).

[69] J.-G. Park, J. D. Forster, and E. R. Dufresne, "Synthesis of colloidal particles with the symmetry of water molecules," Langmuir **25**(16), 8903–8906 (2009).

[70] A. Perro, E. Duguet, O. Lambert, J.-C. Taveau, E. Bourgeat-Lami, and S. Ravaine, "A chemical synthetic route towards 'colloidal molecules,'" Angew. Chem. **121**(2), 367–371 (2009).

[71] B. Peng and A. Imhof, "Surface morphology control of cross-linked polymer particles via dispersion polymerization," Soft Matter **11**(18), 3589–3598 (2015).

[72] J.-B. Fan, H. Liu, Y. Song, Z. Luo, Z. Lu, and S. Wang, "Janus particles synthesis by emulsion interfacial polymerization: Polystyrene as seed or beyond?," Macromolecules **51**(5), 1591–1597 (2018).

[73] I. Lesov, Z. Valkova, E. Vassileva, G. S. Georgiev, K. Ruseva, M. Simeonov, S. Tcholakova, N. D. Denkov, and S. K. Smoukov, "Bottom-up synthesis of polymeric micro-and nanoparticles with regular anisotropic shapes," Macromolecules **51**(19), 7456–7462 (2018).

[74] C. I. Zoldesi, C. A. van Walree, and A. Imhof, "Deformable hollow hybrid silica/siloxane colloids by emulsion templating," Langmuir **22**(9), 4343–4352 (2006).

[75] J. A. Champion, Y. K. Katare, and S. Mitragotri, "Making polymeric micro- and nanoparticles of complex shapes," Proc. Natl. Acad. Sci. U. S. A. **104**(29), 11901–11904 (2007).

[76] H. Shin and C. Kim, "Preparation of spheroidal and ellipsoidal particles from spherical polymer particles by extension of polymer film," Colloid Polym. Sci. **290**(13), 1309–1315 (2012).

[77] Y. Yin, Y. Lu, B. Gates, and Y. Xia, "Template-assisted self-assembly: A practical route to complex aggregates of monodispersed colloids with well-defined sizes, shapes, and structures," J. Am. Chem. Soc. **123**(36), 8718–8729 (2001).

[78] D. Dendukuri, D. C. Pregibon, J. Collins, T. A. Hatton, and P. S. Doyle, "Continuous-flow lithography for high-throughput microparticle synthesis," Nat. Mater. **5**, 365–367 (2006).

[79] J. Guan, N. Ferrell, L. J. Lee, and D. J. Hansford, "Fabrication of polymeric microparticles for drug delivery by soft lithography," Biomaterials **27**(21), 4034–4041 (2006).

[80] G. C. Le Goff, J. Lee, A. Gupta, W. A. Hill, and P. S. Doyle, "High-throughput contact flow lithography," Adv. Sci. **2**(10), 1500149 (2015).

[81] H. Kruggel-Emden, S. Rickelt, S. Wirtz, and V. Scherer, "A study on the validity of the multi-sphere discrete element method," Powder Technol. **188**(2), 153–165 (2008).

[82] D. Markauskas, R. Kačianauskas, A. Džiugys, and R. Navakas, "Investigation of adequacy of multi-sphere approximation of elliptical particles for DEM simulations," Granular Matter **12**(1), 107–123 (2010).

[83] D. Höhner, S. Wirtz, H. Kruggel-Emden, and V. Scherer, "Comparison of the multi-sphere and polyhedral approach to simulate non-spherical particles within the discrete element method: Influence on temporal force evolution for multiple contacts," Powder Technol. **208**(3), 643–656 (2011).